ACS NANO

www.acsnano.org

ARTICLE

Direct Electrical Probing of Periodic Modulation of Zinc-Dopant Distributions in Planar Gallium Arsenide Nanowires

Wonsik Choi,[†,⊗] Eric Seabron,[‡,⊗] Parsian K. Mohseni,[†,#] Jeong Dong Kim,[†] Tobias Gokus,[§] Adrian Cernescu,[§] Pascal Pochet,[⊥,¶] Harley T. Johnson,[⊥,∥] William L. Wilson,[*,‡,▽] and Xiuling Li[*,†,‡,∥]

[†]Department of Electrical and Computer Engineering, Micro and Nanotechnology Laboratory, [‡]Department of Materials Science and Engineering, Fredrick Seitz Materials Research Laboratory, and [∥]Department of Mechanical Science and Engineering, University of Illinois at Urbana−Champaign, Urbana, Illinois 61801, United States

[§]neaspec GmbH, Bunsenstrasse 5, Martinsried, Munich D-821152, Germany

[⊥]Laboratoire de Simulation Atomistique (L_Sim), SP2M, UMR-E CEA/UJF-Grenoble 1, INAC, Grenoble F-38054, France

[▽]Center for Nanoscale Systems, Harvard University, 11 Oxford Street, Cambridge, Massachusetts 02138, United States

Supporting Information

ABSTRACT: **Selective lateral epitaxial (SLE) semiconductor nanowires (NWs), with their perfect in-plane epitaxial alignment, ability to form lateral complex p−n junctions *in situ*, and compatibility with planar processing, are a distinctive platform for next-generation device development. However, the incorporation and distribution of impurity dopants in these planar NWs *via* the vapor−liquid−solid growth mechanism remain relatively unexplored. Here, we present a detailed study of SLE planar GaAs NWs containing multiple alternating axial segments doped with Si and Zn impurities by metalorganic chemical vapor deposition. The dopant profile of the lateral multi-p−n junction GaAs NWs was imaged simultaneously with nanowire topography using scanning microwave impedance microscopy and correlated with infrared scattering-type near-field optical microscopy. Our results provide unambiguous evidence that Zn dopants in the periodically twinned and topologically corrugated p-type segments are preferentially segregated at twin plane boundaries, while Si impurity atoms are uniformly distributed within the n-type segments of the NWs. These results are further supported by microwave impedance modulation microscopy. The density functional theory based modeling shows that the presence of Zn dopant atoms reduces the formation energy of these twin planes, and the effect becomes significantly stronger with a slight increase of Zn concentration. This implies that the twin formation is expected to appear when a threshold planar concentration of Zn is achieved, making the onset and twin periodicity dependent on both Zn concentration and nanowire diameter, in perfect agreement with our experimental observations.**

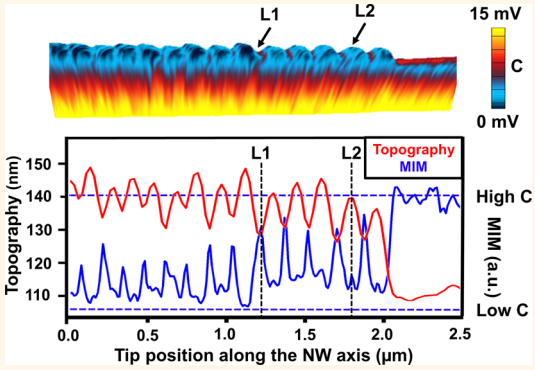

KEYWORDS: *VLS, GaAs, nanowire, MOCVD, selective lateral epitaxy, doping, twin plane defect, sMIM, MIM, nanoIR, IR-sSNOM*

The potential use of nanowire (NW) structures as active components in a multitude of emerging devices is by now well explored. In particular, NWs composed of III−V compound semiconductors potentially have significant impact in numerous technologically relevant fields, and continued research in this area has paved the way for their implementation in next-generation optoelectronic,[1,2] nanoelectronic,[3−6] and photovoltaic applications.[7,8] Although efforts in this realm to date have been predominantly aimed at the manipulation and use of free-standing NWs, which are grown in a bottom-up regime and aligned orthogonally relative to the growth substrate, planar NWs, assembled with lateral alignment along the substrate surface, is gaining considerable research interest due to its excellent material quality and planar processing compatibility.[9−13]

Planar NWs, or NWs grown *via* the selective lateral epitaxy (SLE) approach, are catalyzed by metal nanoparticles according to the vapor−liquid−solid (VLS) or vapor−solid (VS) mechanism and are typically grown within a specific pressure and temperature range that promotes enhanced surface adhesion of the metallic seed particle to substrates,[9−14] and

Received: October 11, 2016
Accepted: January 30, 2017
Published: January 30, 2017

DOI: 10.1021/acsnano.6b06853
ACS Nano 2017, 11, 1530−1539

the [001] direction on GaAs (110) substrates.[15,16] Through the SLE NW growth approach, it has been reported that ZnO NWs are grown in the [1−100] direction on sapphire crystals[9,10] and planar GaN NWs are grown on SiC (0001) parallel to the [1−100], [−1010], and [01−10] surface orientation of the substrate,[11] whereas GaAs planar NWs are grown along the [01−1] or [0−11] surface direction on GaAs (100) substrate.[12−14] One obvious benefit of this technique is the ability to fully exploit conventional planar fabrication technology to realize NW-based devices.[17] This means that no filling medium or planarization thereof is needed for electrical contact formation, which is advantageous from a manufacturing standpoint in comparison to vertical NW arrays. For the purpose of this study, the most notable advantage of this growth mode is the ability to form lateral junctions including p−n junctions and heterojunctions in situ as the NW growth proceeds in-plane along a given crystal orientation. The simplicity through which spatially defined lateral doping profiles can be introduced during planar NW growth represents a strategic advance in crystal growth. Such doping profiles have previously only been achieved through the implementation of labor-intensive processing sequences involving sequential ion implantation or three-dimensional oxide template patterning, followed by selective etching and subsequent growth.

Examples of device applications in nanoelectronics that employ the SLE growth technique include metal−semiconductor field-effect transistors (MESFETs)[18] and metal-oxide semiconductor field-effect transistors (MOSFETs) with single GaAs NW channels,[19] GaAs NW array-based high electron mobility transistors (HEMTs) with record-setting DC and RF performance,[5] simple circuits such as amplifiers,[13] and gate-all-around (GAA) MOSFETs utilizing heteroepitaxially grown planar InAs NWs on GaAs substrates.[20] While the above examples do not require dopant modulation (undoped for HEMTs and n-type doping for MESFETs and MOSFETs), controlled doping of both n-type and p-type, as well as single and multijunction doping profiles, is an important material property underpinning semiconductor device development. Accurate control over the formation of specific dopant distribution profiles, as well as precise and nondestructive methods for the characterization thereof, is imperative. We envision that the incorporation of controlled doping profiles during SLE will enable the use of planar NWs in an extended range of device applications including lateral tunnel-junction FETs, photodetectors and solar cells, light-emitting diodes, and lasers.

Several methods exist for the determination of dopant distribution profiles in semiconductor NWs, including secondary ion mass spectrometry (SIMS)[21] and three-dimensional (3-D) near-atomic-scale spatial resolution *via* atom-probe tomography (APT).[22−28] While both SIMS and APT offer the ability to quantitatively determine concentration of the dopant impurities, these characterization techniques often require complicated and time-consuming specimen preparation steps. Moreover, these techniques provide only the physical concentration of the impurities instead of the electrical carrier concentration. One interesting option lies in the potential for the extraction of dopant distributions from NW structures through the use of nondestructive scanning probe-based techniques, such as Kelvin probe force microscopy (KPFM), scanning capacitance microscopy (SCM), and scanning photocurrent microscopy (SPCM), which have been extensively explored for various nanomaterials.[29−39] While promising, these techniques have several inherent issues that limit their sensitivity to very small electronic perturbations that occur near the sample surface.

Recently, scanning microwave impedance microscopy (sMIM), which uses a specialized coaxial cantilever and a low power (∼10 dB) localized microwave (∼3 GHz) signal to achieve high sensitivity without risking modifying the intrinsic properties of the samples, has been demonstrated as a powerful nondestructive method for the measurement of carrier concentrations.[40,41] Complementary to sMIM imaging, an infrared (IR) scattering-type scanning near-field optical microscopy (IR sSROM) technique has been developed that can spatially map the nanoscale absorption of IR light focused on the sample *via* a tip-induced near-field effect.[42] The IR contrast arises from the Drude absorption of the NW which is directly related to the free carrier concentration introduced by the dopants.[43−45] This method has shown promise in providing dopant profile measurements on NW and nanotube structures.[41]

In this paper, we exploit these two state-of-the-art nanoscale resolution techniques, sMIM and IR-sSNOM, to investigate the distribution profiles of Si (n-type) and Zn (p-type) impurity dopants within individual SLE-grown multijunction GaAs NWs. Through the correlation of AFM topography, sMIM, and IR-sSNOM mapping, we show the preferential incorporation of Zn impurities at the location of twin planes formed within p-type NW segments. To further support our model, we implement a tip voltage modulated variant of MIM called MIM2 to probe for spatial changes in impurity dopant concentration. Density Functional Theory (DFT) modeling shows favorable binding energetics of Zn dopants at twin planes compared with undoped twins, supporting the appearance of laterally twinned planar GaAs NWs upon heavy p-type doping.

RESULTS AND DISCUSSION

Figure 1 shows a representative multi-p−n junction planar GaAs NW and the corresponding flow modulation used during growth. Figure 1a shows a top-view SEM image of the entire NW (∼18 μm long and 250 nm in diameter), with eight distinctly doped n- or p-segments (as labeled) and the Au seed particle at the NW tip, visible on the far right. The corresponding switching scheme (on or off) of MOCVD growth precursors (trimethylgallium [TMGa, $(CH_3)_3Ga$], arsine (AsH_3), disilane (Si_2H_6), and diethylzinc [DEZn, $(C_2H_5)_2Zn$]) during the multiple junction formation is also illustrated in Figure 1a. The periodically corrugated structure in the p-type segments appears as regions of higher contrast due to an increased yield of secondary electrons from the terraced surfaces in these regions. Parts b and c of Figure 1 show higher magnification and 45° tilted views of the second p−n junction (counted from base to tip, from Si- to Zn-doped) segment and the Zn-doped segment near the NW tip, respectively. The Zn-doped segment clearly shows periodically corrugated morphology, in contrast to the smooth morphology in the Si-doped region (left-hand side of image in Figure 1b). We had previously reported on the formation of periodic structural perturbations caused by p-type Zn and C impurities in GaAs planar NWs.[46] As shown in the TEM image in Figure 1d, the corrugation corresponds to the occurrence of (111) twin planes (indicated by black arrows), which sit between the protrusions (red arrows) in the periodic surface topography undulation. For details regarding the crystal structure, the effect of seed particle size on twin periodicity, and evidence of dopant incorporation

DOI: 10.1021/acsnano.6b06853
ACS Nano 2017, 11, 1530−1539

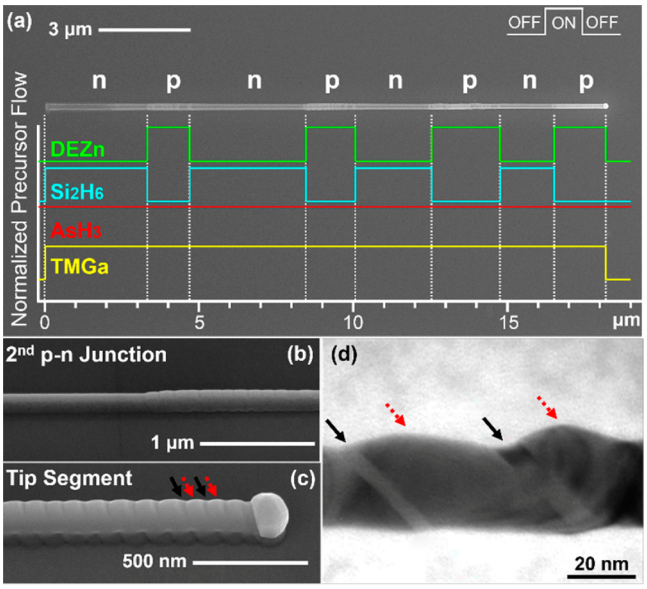

Figure 1. Growth scheme and structure of a planar GaAs nanowire with multiple lateral p−n junctions. (a) Top-view SEM image of a planar multijunction GaAs NW containing alternative n- and p-doped segments, as labeled above the NW. Normalized MOCVD precursor flow rates are superimposed for TMGa (black), AsH_3 (red), Si_2H_6 (blue), and DEZn (green). 45° tilted-view images of the second axial n−p junction (b) and the last Zn-doped p-type segment before the tip of the same NW (c), where the corrugated faceting topography is clearly visible. (d) TEM image (adapted from ref 46) showing the (111) twin planes (black arrows) between the ridges (red dashed arrows) in a Zn-doped planar GaAs NW segment.

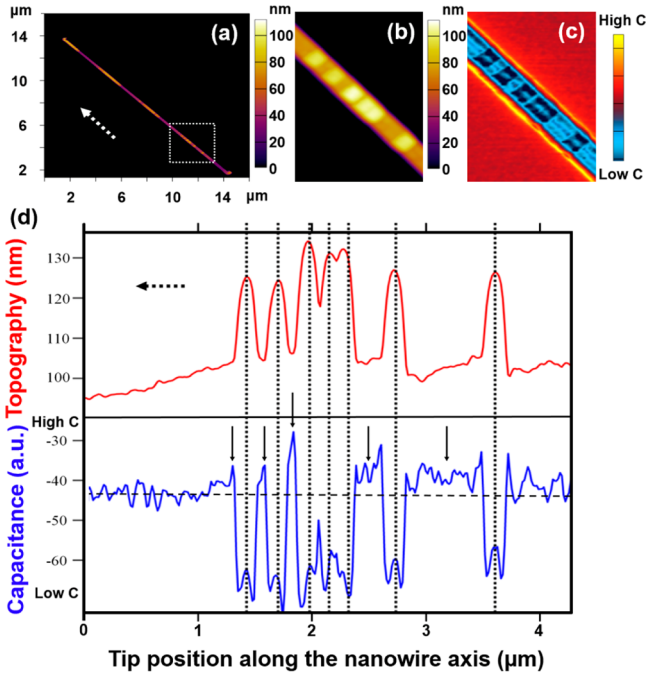

Figure 2. sMIM imaging and line scans of the Zn-doped segment of a p−n junction NW. (a) AFM topography image of the full NW. (b) Topography and (c) MIM capacitance image of the boxed region in (a). (d) Height (red) and capacitance (blue) line scans obtained along the length of the NW segments shown in (b, c). Dotted, vertical lines mark the center of the topography corrugation peaks. The dashed horizontal line shows the baseline capacitance level. Solid black arrows indicate the regions of Zn accumulation (p^+ regions) corresponding to the location of twin planes in the p-type segments of the planar NWs. All dotted arrows point in the growth direction of the NW.

via electrical characterization, we refer readers to ref 46. Next, we map the distribution profiles of impurity dopant species and answer the long-standing research question of doping uniformity and its relationship with twin plane defects in these NWs.

Figure 2a shows an AFM topography map of an eight-segmented, multi-p−n junction planar GaAs NW (the SEM of the same NW was shown in Figure 1a), where the in-plane dimension is in units of micron (μm) and the height (shown as color contrast) is in units of nanometers (nm). The taller regions (orange-tone) are the p-type segments because of the twinned structure and the purple-toned regions represent the n-type segments. In all Figure 2 panels, the dotted arrows point to the NW tip (growth front where the Au particle is located). Parts b and c of Figure 2 show 2-D color maps of the topography and the corresponding capacitance, respectively, of the corrugated p-doped segment in the region outlined by a dashed line box in Figure 2a. The taller corrugated twins appear as regions of higher brightness, with a height difference of approximately 25 nm. It can be seen that the areas with the lowest capacitance (darker blue tone) are precisely located in the distinct corrugation peak regions. The correlation between topography and capacitance can be better viewed in Figure 2d, line scans of the topography and capacitance (imaginary reflectance or sMIM-Im) as a function of position along the NW axis, where the variation in AFM height (top, red curve) and the capacitance (bottom, blue curve) are plotted. The vertical black dotted lines serve as guides to mark the one-to-one correlation of the tallest region of the corrugated p-segment with the valley of capacitance signal, while the solid black arrows denote notable capacitance increase beyond the baseline in the twinned notched regions between the corrugations in the p-type segments. Note that there is also a local maximum in the valley of capacitance (center of the vertical lines). These observations provide spatially resolved evidence at the nanometer scale that the distribution of carriers (holes) in the Zn-doped GaAs NWs is not uniform electrically and indicate that there is an accumulation of free carriers at the twin-plane defects regions and a depletion of free carriers at the corrugation peaks. Note that the high capacitance detected at the NW/substrate interface may originate from the geometrical artifact of sMIM tip[47−49] and the existence of a highly Zn-doped GaAs parasitic thin film under the NW as previously reported by APT measurements normal to the substrate[28] (see the Supporting Information for more explanations).

For comparison, optical amplitude and phase images generated *via* IR-sSNOM mapping along the same segment of the NW of interest are shown in Figure 3. Parts a, c, and e of Figure 3 show topography, optical amplitude, and optical phase images, respectively, of the same multi-n−p planar GaAs NW. The black solid line in Figure 3a, highlighted by the white border, marks the location where the corresponding topography, amplitude, phase profiles were obtained, as shown in Figure 3b,d,e. Line scans obtained from SNOM experiments performed under an 884 cm^{-1} excitation frequency were analyzed. Increased scattering from free charge carriers is qualitatively represented by the local maxima in the optical amplitude profile or by minima in the optical-phase profile,

DOI: 10.1021/acsnano.6b06853
ACS Nano 2017, 11, 1530−1539

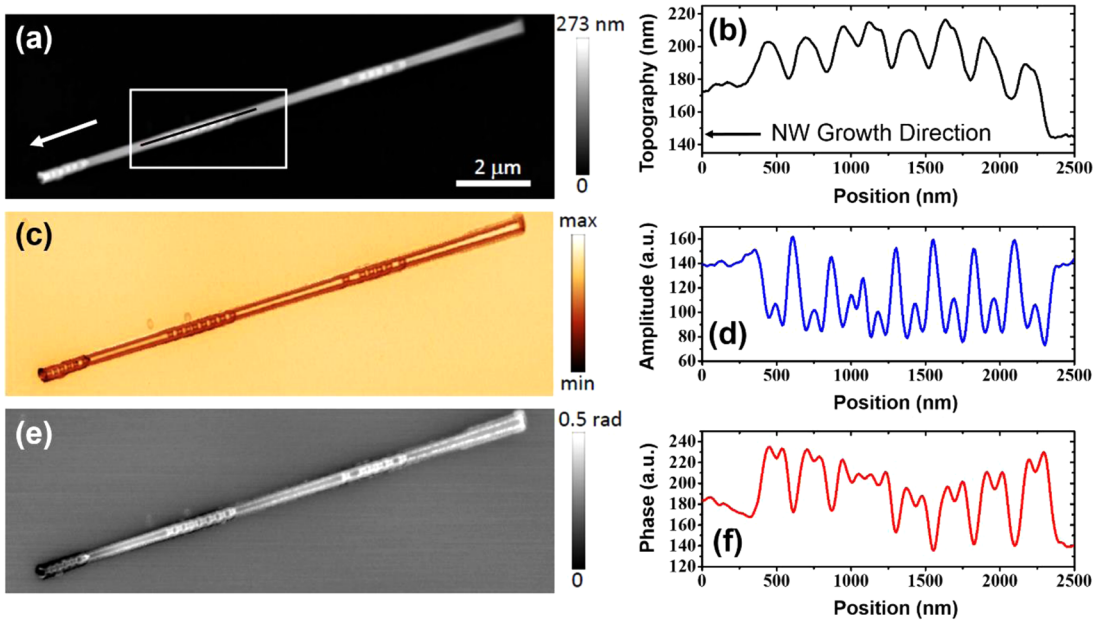

Figure 3. IR near-field mapping of a multiple p-n junction planar GaAs NW at an IR laser frequency of 884 cm^{-1} (11.31 μm wavelength). (a) AFM topography scan and (b) corresponding axial line scan. (c) Near-field amplitude image, directly correlated to the free carrier concentration, and (d) corresponding axial line scan; (e) Near-field phase image and (f) corresponding axial line scan. All line scans were obtained along the black line, highlighted by the white border, in (a). The white and black arrows in (a) and (b) indicate the NW growth direction, respectively.

coincides with the location of twin planes (regions as notches, observed as minima in the topography line scan), in direct agreement with the trend observed in the sMIM data in Figure 2. This highlights the complimentary nature of IR-sSNOM to sMIM and points to preferential localization of Zn dopant impurities along the twin planes.

Based on the sMIM and IR-sSNOM profiles along the Zn-doped p-type NW segments, it can be inferred that the corrugated Zn-doped GaAs NW segment is composed of a series of p–p^+ (peak–notch) homojunctions, as illustrated in Figure 4a in both side view (x–z) and top-down view (x–y). Note that the perfectly symmetric distribution of dopants about the twin boundary illustrated here is an assumption, and measurements such as APT along the NW axis are required to physically map the dopants' location. The areas of greater hole concentration in the twinned notches are denoted as the p^+ region, and the lower hole concentration in the nontwinned raised areas are the p region. The dimensions of the p^+ region (twin plane) and p region (nontwin plane) are assumed to be 4 and 246 nm, respectively, by correlating sMIM capacitance and near-field amplitude line scan results with AFM topography, SEM, and TEM measurements from multiple NWs. Assuming an average Zn doping concentration of 1.67×10^{18} cm^{-3} in the NW (nominal experimental values based on planar control samples) and a volume fraction of 1.6% (4 nm/246 nm) for the p^+ region, we estimate the doping concentration in the p region to be $\sim 7 \times 10^{16}$ cm^{-3} if the p^+ region is to be 1×10^{20} cm^{-3} (the threshold value for twin generation based on the DFT modeling which will be detailed later). Note that all values assumed here are approximations and only used for qualitative trend analysis. Using these values of doping concentrations, the electrostatic potential and electrical field spatial profiles along the NW axis are calculated (details can be found in the SI) and plotted in Figure 4b. The profile can be divided into three regions I–III as indicated in Figure 4b by the arrows. Region I represents the peak potential region centered at the p^+ notch, which drives hole diffusion from the p^+ to p region, leaving behind ionized acceptors in the p^+ region near the p^+–p interface. This forms an accumulation of holes in the p region near the junction. However, due to the carrier continuity of the homojunction, the p^+ region is not fully depleted, so a larger number of free carriers remain in the charge neutral region of the p^+ side. This agrees with the observations of high sMIM capacitance and high IR-sSNOM amplitude signals in the notch regions. In region II, holes are localized by the strong internal fields, forming a space charge region, which suppresses their contribution to Coulomb screening at the sample surface just below the tip. Considering that holes in this region cannot be treated like truly free carriers, the surface capacitance in region II should be reduced. The steep decline in the MIM capacitance signal observed exactly at the *onset* of the topographical corrugation peak (Figure 2d) is consistent with the presence of this space charge region. Region III is the quasi-flatband region in the lower doped p-region where the holes do not experience strong localizing E-fields; hence, they behave like free carriers. This model explains the small but distinct spike in capacitance located in the middle of the deep capacitance valley (Figure 2d), which is spatially correlated with the *center* of the topological corrugation peak region. Figure 4c is an expanded view of region I (p^+ notch) to highlight the flat band region in the center of the potential well, where the charge neutrality means the holes are also free carriers, except with a much higher concentration than in region III. This agrees completely with the observed capacitance peaks indicated by the black arrows in Figure 2d.

The physical model presented above can further be supported by bias-modulated microwave impedance microscopy (MIM2) measurements. In the MIM2 measurement, the Fermi energy level at the surface is influenced by the tip bias modulated at a fixed frequency (~90 kHz); the tip bias has a

DOI: 10.1021/acsnano.6b06853
ACS Nano 2017, 11, 1530–1539

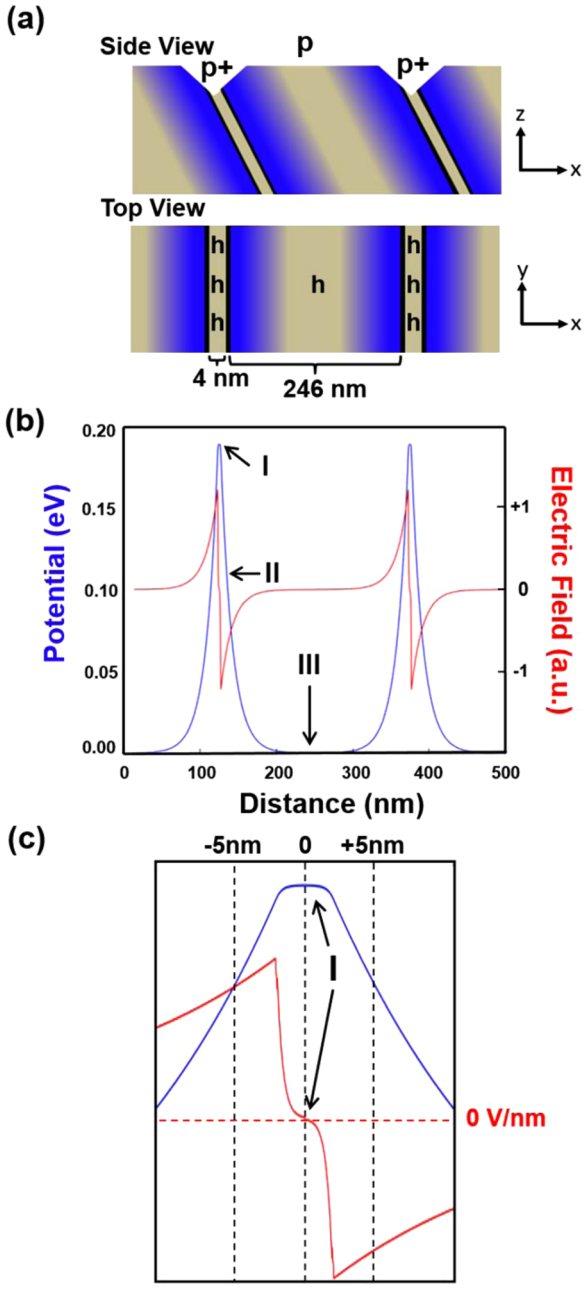

Figure 4. Physical model of the spatial distribution of carriers in the p region with twin-planes. (a) Illustration of the physical geometry along the NW corrugations used for numerical calculation. The blue regions represent areas of space charge regions. (b) Plot of the numerical calculation of the potential (blue, left axis) and E-field (red, right axis) along the NW axial direction, *x*. Three regions identified as I, II, and III represent the highly doped (p^+) hole potential well, space charge region with high E-fields, and the lower doped (p) flat band region. (c) Expanded view of region I (re-centered so that $x = 0$ as labeled) in Figure 4b where the hole potential well shows as an area of flat band potential and zero E-field at $x = 0$.

fully offset sine waveform that oscillates between 0 and V_{tip}.[41] The experimental geometry for measuring the differential capacitance *via* MIM2 is similar to that of scanning capacitance microscopy (SCM) where the tip−semiconductor interface forms a gating structure that when biased can cause population inversion or depletion directly underneath the tip. The simple interpretation of the capacitance signal is that it mimics semiconductor C−V curves, which have been shown, in previous experiments with SCM, to have weaker voltage dependence at higher doping concentrations.[50−52] Since we are measuring a differential signal, the average slope of the C−V curve from $V = 0$ to V_{tip} gives rise to the observed MIM2 signal. By applying the tip bias, it is possible to compensate for the internal fields in a carrier depletion region; the charge stored in the region from ionized dopants and excess charge carriers manifests as a flat-band voltage shift in the C−V curves such that a stronger bias is needed to achieve a notable change in the population of free carriers (*i.e.*, population inversion or accumulation).[53,54] We hypothesize that both the overall dopant concentration and the presence of internal E-fields (space charge) will impact the MIM2 response. Parts a−c of Figure 5 show three spatial profiles of capacitance images (overlaid with topography) obtained from the same single junction NW on the Zn-doped side of the p−n junction under conventional MIM (grounded tip) and MIM2 with a V_{tip} of −3 and −9 V, respectively. Figure 5d shows the corresponding line scans, including AFM topography, as labeled. Note that shown in Figure 5b,c are the differential capacitances under the corresponding bias where the dark blue color indicates near-zero response to the modulated tip voltage, while green to yellow color shows increasing sensitivity to the modulated voltage. At V_{tip} = −3 V (Figure 5b), the modulated tip bias shows minimum effect on the measured capacitance everywhere except a small area in the center of the lower doped flatband region, while at V_{tip} = −9 V (Figure 5c) dramatic localized changes in capacitance can be seen everywhere except the highly doped p^+ region. For instance, L1 (the valley in the periodic topography corrugation as indicated by arrows in Figure 5) is characterized by the clear increase in MIM capacitance and a lack of MIM2 response observed; while L2 (the center of the peak region in the periodic topography) shows a localized maximum in the MIM capacitance and a strong peak in MIM2 especially under the higher modular tip bias (V_{tip} = −9 V). Based on the physical model (Figure 4), we expect the space charge region (p-side of region II) and the flatband region (center of the p-region, region III) to show a strong response to high tip bias (−9 V) since they have a smaller dopant concentration. However, the presence of internal E-fields in the space charge region (region II) would cause a voltage shift in the C−V response that suppresses the differential capacitance signal at low tip bias (−3 V). On the other hand, the capacitance in the middle of a highly doped p^+ region (region I) would be minimally affected by the tip bias because of the higher dopant concentration and strong local E-fields that interact with the charge carriers, preventing the free carriers from locally redistributing to compensate for the modular tip bias. MIM2 observations are completely consistent with the physical model of spatial distribution of carriers in the NW presented in Figure 4.

A spatial correlation between impurity species and defects in NWs has been reported previously in several studies. Hemesath *et al.* showed direct evidence of impurity Au atoms and their preferential incorporation along the grain boundaries of Si NWs having ⟨110⟩ growth directions.[55] Prominent twinning was also observed during growth of one-dimensional, Sb-doped ZnO nanostructures.[56] In fact, it was later shown that Sb doping can lead to a kinking of the ZnO NW morphology at the site of twin planes.[57] Furthermore, dramatic changes in crystal structure were shown to take place during Zn doping of both

DOI: 10.1021/acsnano.6b06853
ACS Nano 2017, 11, 1530−1539

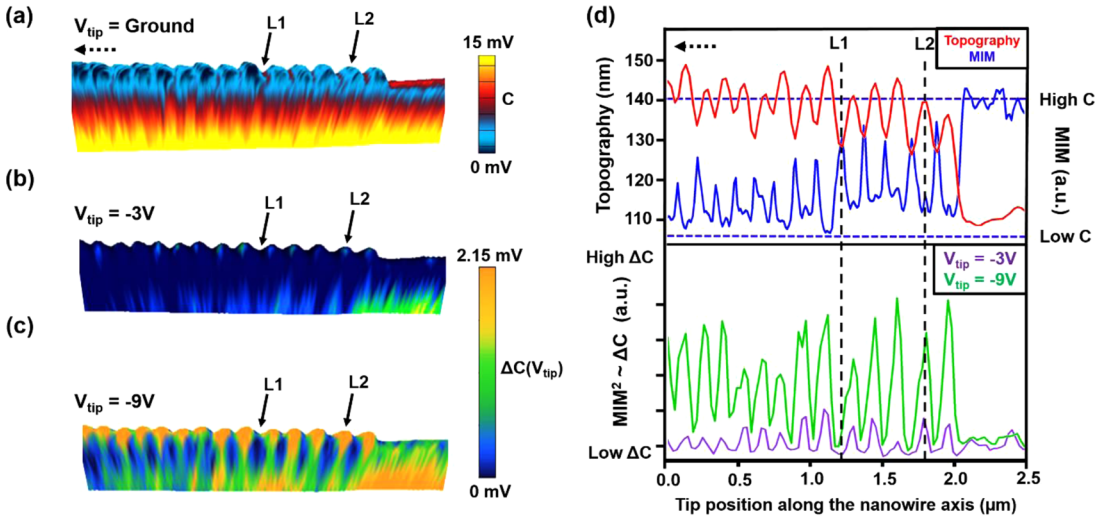

Figure 5. Conventional MIM and tip voltage modulated MIM (MIM2) of the Zn-doped segment of a single p−n junction planar GaAs NW. (a−c) Overlay of data represented in color onto a 3D view of NW topography. Dotted arrows in (a) and (b) indicate the growth direction of NW. (a) Contact mode MIM color scheme. All MIM2 data were taken with a tip modulation in sine waveform varying between 0 and V_{tip} at 90 kHz; they both have the same color scale where areas with zero response are dark blue and higher sensitivity to the modulated voltage is shown in yellow. (b) MIM2 data taken at V_{tip} = −3 V (c) MIM2 data taken at V_{tip} = −9 V. (d) Plot of several line cuts down the axis of the NW of the topography (top, left axis, red), MIM capacitance (middle, right axis, blue), and MIM2 data offset to zero (bottom, left axis, green and purple). Arrows and vertical lines mark the spatial location and the corresponding data that are consistent across all forms of measurements: L1 is a potential well formed from the highly Zn doped p^+ region in the notches, and L2 is the flat band region that exists at the center of the peaks.

Table I. DFT Calculation Results[a]

	1 Zn	2 Zn	3 Zn	6 Zn
bulk conc (cm^{-3})	1.0×10^{20}	2.0×10^{20}	3.0×10^{20}	5.9×10^{20}
planar conc (nm^{-2})	2.0×10^{-1}	3.9×10^{-1}	5.9×10^{-1}	11.8×10^{-1}
$E_{\text{In-plane binding}}$ (meV)	0	−27	−82	−464
$E_{\text{twin binding}}$ (A/B) (meV)	−32/−25	−51/−37	−77/−55	−82/NC
$E_{\text{Total binding}}$ (A/B) (meV)	−32/−25	−78/−64	−159/−137	−525/NC
max E reduction (%)	3	7	15	50

[a]Bulk concentrations are in cm^{-3}, planar concentrations are in nm^{-2}, binding energies are in meV, and reductions are in %. (A/B) denotes the (111)A or (111)B face of GaAs; the twins are oriented along (111)B. NC: not calculated. The addition of Zn reduces the formation energy of the twin boundary through (i) a binding energy between Zn atoms and (ii) a binding energy between the Zn and the twin.

twinned superlattice InP[58] and kinked, polytypic GaN NWs.[59] Lastly, we note that Chen *et al.* have reported on the localization of seed particle impurities, during In/Sb alloy-assisted growth, at twin plane defects in Si NWs.[60] It was proposed in their study that uniform incorporation of impurity species precedes their preferential segregation at the site of twin planes and that the likelihood for localization at a defect site is proportional to the segregation energy of the impurity species.

The MIM and IR-sSNOM results above provided clear evidence that that Zn doping in VLS grown planar GaAs NWs is not uniform: there is strong local accumulation of Zn dopants, and the presence or accumulation of Zn is associated with [111] twinning in the planar GaAs NWs studied here. However, the nature of the mechanism through which this process proceeds warrants further theoretical consideration. Using the BigDFT electronic structure code,[61,62] the effect of Zn dopant atoms on the formation energy of these twins is analyzed. We construct an orthorhombic, periodic 432-atom unit cell, approximately 2.1 × 2.4 × 2.0 nm, containing a pair of GaAs twins. The calculation parameters are chosen in accordance with those reported previously for similar semiconductor materials:[63] the exchange-correlation energy is handled *via* the generalized gradient approximation (GGA) with HGH pseudopotential and a Brillouin zone integration at the Γ point. The structural relaxations use the FIRE algorithm with an energy convergence criterion of 3 meV/Å. The energy of the twin boundary in undoped GaAs is found to be 2.05 eV/$Å^2$, which is in good agreement with previous experimental measurements,[64] and relatively low among III−V semiconductors. As shown in Table I, the formation energy of the same boundary in GaAs doped with 1% Zn or 10^{20} cm^{-3}, in the A-type (B-type) polarity, is reduced by roughly 3% (2%). One arrives at these numbers by comparing the energy of the twin in the doped case with the energy of GaAs, without a twin, at the same Zn concentration.

The thermodynamic chemical potential is defined in terms of the Zn−As pair and defined by the energy difference between a pure GaAs system and the GaAs system with 1% Zn that contains one Zn−As pair substituting for a Ga−As pair. When a twin is present, and the Zn substitution is at the twin boundary, there is further energy reduction with additional Zn concentration. As shown in Table I, this holds beyond the average concentration level of 1%, or approximately 10^{20} cm^{-3}. The energy reduction, in fact, has a stronger-than-linear dependence on Zn concentration. This result can be considered as the thermodynamic measure of the defect formation energy

DOI: 10.1021/acsnano.6b06853
ACS Nano 2017, 11, 1530−1539

reduction due to Zn when substitutional Zn is taken as a reference for Zn.

While the calculation results suggest that there is a non-negligible binding (or energy reduction due to spatial proximity) between the Zn dopants and a GaAs twin, one must also consider the relationship between the overall spatial distribution of Zn and the relatively distantly spaced twins found in the planar GaAs NWs. Since twinning is experimentally observed only when the nominal doping concentration is above the 10^{18} cm^{-3} range,[46] Zn is only likely to promote twinning by reducing the twin formation energy if there is a sufficient spatial nonuniformity in the Zn distribution, so that locally the Zn concentrations can approach the 10^{19}–10^{20} cm^{-3} level considered in the computational study. Indeed, previous experimental evidence suggests that there is a many-body effect by which Zn dopant atoms in GaAs segregate due to an attractive interaction.[65] In the present case, if a modest segregation effect shifts the average Zn concentration of 10^{18} to a local concentration that is an order of magnitude higher, as seen by Ebert *et al.*,[65] the strong twin formation energy reduction seen in the present calculations would provide a clear explanation of the experimentally observed twins. Thus, the Zn-induced twinning in GaAs may be driven by a two-step mechanism, as shown by the results of the calculations: first the Zn impurities segregate due to a negative binding energy (calculated to be 82 meV in our unit cell containing three Zn atoms, Table I), and second, the twin forms due to an additional energy reduction of the twin in the presence of the Zn-enriched plane (calculated to be 77 meV for three Zn atoms, Table I). Overall, in this case, the twin formation is reduced by about 15% with respect to the undoped case. The three Zn atom case, considered here as an example to illustrate the role of the Zn planar concentration, corresponds to a Zn planar density of 0.59 nm^{-2} (or 5.9×10^{13} cm^{-2}). It is also interesting to note that the effect becomes significantly stronger at slightly higher Zn concentrations; in the six-Zn-atom case, for example, the total energy reduction reaches 50%, most of which is due to the in-plane binding of the Zn dopant atoms. Given such a correlation, the twin is expected to appear when a threshold concentration is achieved. That was indeed what was observed experimentally,[46] where the onset of twin-plane superlattice (TSL) formation in planar Zn-doped GaAs NWs was estimated to be around the 10^{19} cm^{-3} doping level based on electrical measurements.

CONCLUSIONS

In summary, using the state-of-the-art, nondestructive, tip-based scanning microscopy techniques, MIM, MIM2, and IR-sSNOM, we have probed the dopant distribution profile in multijunction planar GaAs NWs grown by Au-seeded SLE mechanism. By the one-to-one correlation of the topography, electrical carrier distribution, and dopant impurity scattering profiles, we have provided unambiguous evidence that Zn dopants are preferentially accumulated at the twin-plane boundaries. We attribute this phenomenon to an energy driven mechanism where having Zn impurities residing in the twin planes lowers the twin formation energy, as confirmed by DFT calculations.

METHODS

NW Growth. Sample preparation for NW growth was initiated by surface cleaning of semi-insulating (SI) GaAs (100) substrates with resistivity of >1E7 Ω·cm in a diluted solution of hydrochloric acid and deionized water (volumetric dilution ratio of 1:1) for the removal of surface oxide layers and residual organic contaminants. Next, monodispersed Au colloids (BBI solutions) with 250 nm diameters were drop-cast onto the GaAs surface, and samples were loaded in a horizontal-flow configuration 200/4 AIXTRON MOCVD reactor for SLE-NW growth. Prior to the onset of growth, a surface oxide desorption step at 650 °C was implemented for a period of 10 min under an arsine (AsH_3) flow of 50 sccm. The supply of TMGa, AsH_3, Si_2H_6, and DEZn precursor gases provided group III, group V, n-type dopant, and p-type dopant growth species, respectively, under a constant hydrogen (H_2) carrier gas flow of 5 L/min. Planar NW growth was carried out at a temperature of 460 °C for a total duration 160 s at a reactor pressure of 950 mbar. During the multijunction NW growth, the supply of Si_2H_6 and DEZn was alternated 8 times, with dopant precursor flows monotonically increasing in each sequentially grown segment, resulting in the lateral assembly of 4 n–p (also, 3 p–n) junctions along the axial growth direction. Based on calibrations of GaAs (100) thin films, Si concentrations in the alternating n-type segments are estimated as 1.63×10^{17}, 4.47×10^{17}, 4.71×10^{18}, and 9.45×10^{18} cm^{-3}, while Zn concentrations in the alternating p-type NW segments are estimated to be 1.67×10^{18}, 3.33×10^{18}, 5.33×10^{18}, and 6.00×10^{18} cm^{-3} from NW base to tip. Growth was terminated after the formation of the final p-type segment through the cessation of TMGa and DEZn supply, and the samples were cooled under a constant AsH_3 flow. After removal from the growth reactor, the samples were subjected to a short (5 s) etching process in a solution of $H_2SO_4/H_2O_2/H_2O$ (1:8:340) for the removal of a ∼20 nm parasitic thin film on the 18 μm long NW sample surface, which was formed in tandem with NW growth both on the NW sidewalls and in the exposed substrate surfaces between NWs under this growth condition. We note that this postepitaxy etching process does not adversely influence the morphology or structure of the laterally grown NWs, nor does it modify the distribution of dopants therein.

Postgrowth Inspection of NWs. Postgrowth inspection was performed using a Hitachi S-4800 field-emission scanning electron microscopy (SEM) system and JEOL 2010 LaB6 transmission electron microscope (TEM), and the locations of individual NWs of interest were marked and mapped using an FEI Helios NanoLab 600i focused ion beam (FIB) system for subsequent correlation of sMIM and IR-sSNOM data.

sMIM Mapping of NWs. All sMIM experiments were performed using PrimeNano, Inc., microwave detection electronics, tip holders, and custom coaxial tips in conjunction with an Asylum MFP3D atomic force microscope. All AFM–MIM analysis was done on as-grown samples in a contact mode scanning geometry. For this setup, the microwave signal propagates from the source (−10 dB, 2.7–3.3 GHz) to the apex of the coaxial tip where a portion of the signal reflected back according to the sample impedance. The imaginary part of the microwave reflectivity was isolated using a capacitive standard calibration sample, alumina (Al_2O_3) dots on silicon, making the technique sensitive to small changes in surface capacitance. The MIM-Im signal is proportional to the tip–sample capacitance resulting from charge stored in the metal–semiconductor junction formed in the contact mode geometry.[40] The capacitance data can be qualitatively correlated to the inverse of the Debye screening length under the tip, which is linearly proportional to the square root of the free carrier concentration ($n^{1/2}$), according to a simple physical interpretation of the depletion capacitance at metal–semiconductor junctions. Other contributions to the capacitance signal such as thermal drift from internal electronics and environmental stray capacitance creates an arbitrary baseline signal that must be normalized using a linear flatten filter; this makes the technique qualitative in nature.

IR-sSNOM Mapping of NWs. IR near-field maps of individual NWs were acquired by utilizing a commercially available SNOM microscope (neaSNOM, neaspec GmbH). Here the output of a continuous-wave tunable CO_2-laser (Access laser) at a frequency of 884 cm^{-1} was focused *via* a parabolic mirror on to a Pt/Ir coated Si-AFM tip (Arrow NCPT, Nanoworld) with an apex radius of ca. 20 nm. While scanning, the sample below the AFM tip, we detect and analyze the tip-scattered light using a Michelson interferometer to obtain

DOI: 10.1021/acsnano.6b06853
ACS Nano 2017, 11, 1530–1539

simultaneous optical amplitude and phase maps of the NWs. In order to eliminate far-field background scattering, the AFM is operated in dynamic mode where the tip oscillated at an amplitude of about 40–50 nm at a frequency $\Omega \sim 250$ kHz allowing interferometric heterodyne detection of the apetureless nearfield signal. The details of the optical signal processing technique can be found in.[42] The optical detector signal is demodulated at higher harmonics of the tip oscillation frequency (~3–4 $n\Omega$), yielding background-free IR near-field amplitude and phase signals. According to the Drude model, the optical absorption in the mid-IR is proportional to the free carrier concentration; hence, spatial changes in the near-field amplitude signal is dominated by the surface's free carrier distribution.[45] This makes IR-sSNOM characterization a directly complementary to MIM for electron property mapping.

ASSOCIATED CONTENT

Supporting Information

The Supporting Information is available free of charge on the ACS Publications website at DOI: 10.1021/acsnano.6b06853.

Scanning microwave impedance microscopy observable, possible geometrical artifacts of sMIM and high sMIM capacitance along the interface between the NW and substrate, and numerical and qualitative analysis of charge distribution in Zn-doped GaAs NW (PDF)

AUTHOR INFORMATION

Corresponding Authors

*E-mail: xiuling@illinois.edu.

*E-mail: wwilson@cns.fas.harvard.edu.

ORCID

Wonsik Choi: 0000-0001-8550-0175

Present Addresses

[#](P.K.M.) Microsystems Engineering, Rochester Institute of Technology, Rochester, NY 14623.

[¶](P.P.) Univ. Grenoble Alpes, F-38000 Grenoble, France and Atomistic Simulation Laboratory (L_Sim), CEA, INAC, F-38054, Grenoble, France.

Author Contributions

[⊗]W.C. and E.S. contributed equally to this work.

Notes

The authors declare no competing financial interest.

ACKNOWLEDGMENTS

We acknowledge financial support by NSF DMR Award No. 1508140. We thank Scott MacLaren at Fredrick Seitz Materials Research Laboratory for technical assistance. H.T.J. acknowledges support from a Fulbright Fellowship and from Universite Joseph Fourier, Grenoble, through an invited professorship. The DFT calculations were performed using French supercomputers GENCI-CINES and GENCI-CCRT through project 6194.

REFERENCES

(1) Eaton, S. W.; Fu, A.; Wong, A. B.; Ning, C.-Z.; Yang, P. Semiconductor Nanowire Lasers. *Nat. Rev. Mater.* **2016**, *1*, 16028.

(2) Saxena, D.; Wang, F.; Gao, Q.; Mokkapati, S.; Tan, H. H.; Jagadish, C. Mode Profiling of Semiconductor Nanowire Lasers. *Nano Lett.* **2015**, *15*, 5342–5348.

(3) Zhang, C.; Li, X. III-V Nanowire Transistors for Low-Power Logic Applications: A Review and Outlook. *IEEE Trans. Electron Devices* **2016**, *63*, 223–234.

(4) Schmid, H.; Borg, M.; Moselund, K.; Gignac, L.; Breslin, C. M.; Bruley, J.; Cutaia, D.; Riel, H. Template-Assisted Selective Epitaxy of III–V Nanoscale Devices for Co-Planar Heterogeneous Integration with Si. *Appl. Phys. Lett.* **2015**, *106*, 233101.

(5) Miao, X.; Chabak, K.; Zhang, C.; Mohseni, P. K.; Walker, D.; Li, X. High-Speed Planar GaAs Nanowire Arrays with fmax > 75 GHz by Wafer-Scale Bottom-up Growth. *Nano Lett.* **2015**, *15*, 2780–2786.

(6) Svensson, J.; Dey, A. W.; Jacobsson, D.; Wernersson, L.-E. III–V Nanowire Complementary Metal–Oxide Semiconductor Transistors Monolithically Integrated on Si. *Nano Lett.* **2015**, *15*, 7898–7904.

(7) LaPierre, R. R.; Chia, A. C. E.; Gibson, S. J.; Haapamaki, C. M.; Boulanger, J.; Yee, R.; Kuyanov, P.; Zhang, J.; Tajik, N.; Jewell, N.; Rahman, K. M. A. III–V Nanowire Photovoltaics: Review of Design for High Efficiency. *Phys. Status Solidi RRL* **2013**, *7*, 815–830.

(8) Åberg, I.; Vescovi, G.; Asoli, D.; Naseem, U.; Gilboy, J. P.; Sundvall, C.; Dahlgren, A.; Svensson, K. E.; Anttu, N.; Björk, M. T.; Samuelson, L. A GaAs Nanowire Array Solar Cell with 15.3% Efficiency at 1 Sun. *IEEE J. Photovoltaics.* **2016**, *6*, 185–190.

(9) Nikoobakht, B.; Wang, X.; Herzing, A.; Shi, J. Scalable Synthesis and Device Integration of Self-Registered One-Dimensional Zinc Oxide Nanostructures and Related Materials. *Chem. Soc. Rev.* **2013**, *42*, 342–365.

(10) Nikoobakht, B. Toward Industrial-Scale Fabrication of Nanowire-Based Devices. *Chem. Mater.* **2007**, *19*, 5279–5284.

(11) Tsivion, D.; Joselevich, E. Guided Growth of Epitaxially Coherent GaN Nanowires on Sic. *Nano Lett.* **2013**, *13*, 5491–5496.

(12) Fortuna, S. A.; Wen, J.; Chun, I. S.; Li, X. Planar GaAs Nanowires on GaAs (100) Substrates: Self-Aligned, Nearly Twin-Defect Free, and Transfer-Printable. *Nano Lett.* **2008**, *8*, 4421–4427.

(13) Zhang, C.; Dowdy, R.; Li, X. High Voltage Gain MESFET Amplifier Using Self-Aligned MOCVD Grown Planar GaAs Nanowires. *Device Research Conference (DRC)* **2013**, 63–64.

(14) Zhang, C.; Miao, X.; Mohseni, P. K.; Choi, W.; Li, X. Site-Controlled VLS Growth of Planar Nanowires: Yield and Mechanism. *Nano Lett.* **2014**, *14*, 6836–6841.

(15) Dowdy, R.; Walko, D.; Fortuna, S. A.; Li, X. Realization of Unidirectional Planar GaAs Nanowires on (110) Substrates. *IEEE Electron Device Lett.* **2012**, *22* (4), 522–524.

(16) Dowdy, R.; Walko, D.; Li, X. Relationship between plannar GaAs nanowire growth direction and substrate orientation. *Nanotechnology* **2013**, *24*, 035304.

(17) Tsivion, D.; Schvartzman, M.; Popovitz-Biro, R.; von Huth, P.; Joselevich, E. Guided Growth of Millimeter-Long Horizontal Nanowires with Controlled Orientations. *Science* **2011**, *333*, 1003–1007.

(18) Fortuna, S. A.; Li, X. In GaAs FET with a High Mobility Self-Assembled Planar Nanowire Channel on a (100) Substrate. *Device Research Conference (DRC)* **2009**, 19–20.

(19) Zhang, C.; Li, X. Planar GaAs Nanowire Tri-Gate MOSFETs by Vapor–Liquid–Solid Growth. *Solid-State Electron.* **2014**, *93*, 40–42.

(20) Zhang, C.; Choi, W.; Mohseni, P. K.; Li, X. InAs Planar Nanowire Gate-All-Around MOSFETs on GaAs Substrates by Selective Lateral Epitaxy. *IEEE Electron Device Lett.* **2015**, *36*, 663–665.

(21) Chia, A. C. E.; Boulanger, J. P.; LaPierre, R. R. Unlocking Doping and Compositional Profiles of Nanowire Ensembles Using SIMS. *Nanotechnology* **2013**, *24*, 045701.

(22) Roussel, M.; Chen, W.; Talbot, E.; Lardé, R.; Cadel, E.; Gourbilleau, F.; Grandidier, B.; Stiévenard, D.; Pareige, P. Atomic Scale Investigation of Silicon Nanowires and Nanoclusters. *Nanoscale Res. Lett.* **2011**, *6*, 271.

(23) Perea, D. E.; Hemesath, E. R.; Schwalbach, E. J.; Lensch-Falk, J. L.; Voorhees, P. W.; Lauhon, L. J. Direct Measurement of Dopant Distribution in an Individual Vapour-Liquid-Solid Nanowire. *Nat. Nanotechnol.* **2009**, *4*, 315–319.

(24) Moutanabbir, O.; Isheim, D.; Blumtritt, H.; Senz, S.; Pippel, E.; Seidman, D. N. Colossal Injection of Catalyst Atoms into Silicon Nanowires. *Nature* **2013**, *496*, 78–82.

(25) Xu, T.; Nys, J. P.; Grandidier, B.; Stiévenard, D.; Coffinier, Y.; Boukherroub, R.; Larde, R.; Cadel, E.; Pareige, P. Growth of Si Nanowires on Micropillars for the Study of Their Dopant Distribution

DOI: 10.1021/acsnano.6b06853
ACS Nano 2017, 11, 1530–1539

by Atom Probe Tomography. *J. Vac. Sci. Technol., B* **2008**, *26*, 1960−1963.
(26) Du, S.; Burgess, T.; Gault, B.; Gao, Q.; Bao, P.; Li, L.; Cui, X.; Kong Yeoh, W.; Liu, H.; Yao, L.; Ceguerra, A. V.; Hoe Tan, H.; Jagadish, C.; Ringer, S. P.; Zheng, R. Quantitative Dopant Distributions in GaAs Nanowires Using Atom Probe Tomography. *Ultramicroscopy* **2013**, *132*, 186−192.
(27) Agrawal, R.; Bernal, R. A.; Isheim, D.; Espinosa, H. D. Characterizing Atomic Composition and Dopant Distribution in Wide Band Gap Semiconductor Nanowires Using Laser-Assisted Atom Probe Tomography. *J. Phys. Chem. C* **2011**, *115*, 17688−17694.
(28) Qu, J.; Choi, W.; Katal Mohseni, P.; Li, X.; Zhang, Y.; Chen, H.; Ringer, S.; Zheng, R. Direct Observation of Dopants Distribution and Diffusion in GaAs Planar Nanowires with Atom Probe Tomography. *ACS Appl. Mater. Interfaces* **2016**, *8*, 26244−26250.
(29) Koren, E.; Rosenwaks, Y.; Allen, J. E.; Hemesath, E. R.; Lauhon, L. J. Nonuniform Doping Distribution Along Silicon Nanowires Measured by Kelvin Probe Force Microscopy and Scanning Photocurrent Microscopy. *Appl. Phys. Lett.* **2009**, *95*, 092105.
(30) Koren, E.; Hyun, J. K.; Givan, U.; Hemesath, E. R.; Lauhon, L. J.; Rosenwaks, Y. Obtaining Uniform Dopant Distributions in VLS-Grown Si Nanowires. *Nano Lett.* **2011**, *11*, 183−187.
(31) Kikukawa, A.; Hosaka, S.; Imura, R. Silicon PN Junction Imaging and Characterizations Using Sensitivity Enhanced Kelvin Probe Force Microscopy. *Appl. Phys. Lett.* **1995**, *66*, 3510−3512.
(32) Allen, J. E.; Perea, D. E.; Hemesath, E. R.; Lauhon, L. J. Nonuniform Nanowire Doping Profiles Revealed by Quantitative Scanning Photocurrent Microscopy. *Adv. Mater.* **2009**, *21*, 3067−3072.
(33) Kelzenberg, M. D.; Turner-Evans, D. B.; Kayes, B. M.; Filler, M. A.; Putnam, M. C.; Lewis, N. S.; Atwater, H. A. Photovoltaic Measurements in Single-Nanowire Silicon Solar Cells. *Nano Lett.* **2008**, *8*, 710−714.
(34) Gu, Y.; Romankiewicz, J. P.; David, J. K.; Lensch, J. L.; Lauhon, L. J.; Kwak, E.-S.; Odom, T. W. Local Photocurrent Mapping as a Probe of Contact Effects and Charge Carrier Transport in Semiconductor Nanowire Devices. *J. Vac. Sci. Technol., B* **2006**, *24*, 2172−2177.
(35) Gu, Y.; Kwak, E.-S.; Lensch, J. L.; Allen, J. E.; Odom, T. W.; Lauhon, L. J. Near-Field Scanning Photocurrent Microscopy of a Nanowire Photodetector. *Appl. Phys. Lett.* **2005**, *87*, 043111.
(36) Narváez, A. C.; Chiaramonte, T.; Vicaro, K. O.; Clerici, J. H.; Cotta, M. A. Evidence of Space Charge Regions within Semiconductor Nanowires from Kelvin Probe Force Microscopy. *Nanotechnology* **2009**, *20*, 465705.
(37) Ono, S.; Takeuchi, M.; Takahashi, T. Current and Potential Characterization on InAs Nanowires by Contact-Mode Atomic Force Microscopy and Kelvin Probe Force Microscopy. *Ultramicroscopy* **2002**, *91*, 127−132.
(38) Vinaji, S.; Lochthofen, A.; Mertin, W.; Regolin, I.; Gutsche, C.; Prost, W.; Tegude, F. J.; Bacher, G. Material and Doping Transitions in Single GaAs-Based Nanowires Probed by Kelvin Probe Force Microscopy. *Nanotechnology* **2009**, *20*, 385702.
(39) Sommerhalter, C.; Matthes, T. W.; Glatzel, T.; Jäger-Waldau, A.; Lux-Steiner, M. C. High-Sensitivity Quantitative Kelvin Probe Microscopy by Noncontact Ultra-High-Vacuum Atomic Force Microscopy. *Appl. Phys. Lett.* **1999**, *75*, 286−288.
(40) Kundhikanjana, W.; Yang, Y.; Tanga, Q.; Zhang, K.; Lai, K.; Ma, Y.; Kelly, M. A.; Li, X. X.; Shen, Z. X. Unexpected Surface Implanted Layer in Static Random Access Memory Devices Observed by Microwave Impedance Microscope. *Semicond. Sci. Technol.* **2013**, *28*, 025010.
(41) Seabron, E.; MacLaren, S.; Xie, X.; Rotkin, S. V.; Rogers, J. A.; Wilson, W. L. Scanning Probe Microwave Reflectivity of Aligned Single-Walled Carbon Nanotubes: Imaging of Electronic Structure and Quantum Behavior at the Nanoscale. *ACS Nano* **2016**, *10*, 360−368.
(42) Atkin, J. M.; Berweger, S.; Jones, A. C.; Raschke, M. B. Nano-Optical Imaging and Spectroscopy of Order, Phases, and Domains in Complex Solids. *Adv. Phys.* **2012**, *61*, 745−842.
(43) Huber, A. J.; Wittborn, J.; Hillenbrand, R. Infrared Spectroscopic Near-Field Mapping of Single Nanotransistors. *Nanotechnology* **2010**, *21*, 235702.
(44) Keilmann, F.; Huber, A. J.; Hillenbrand, R. Nanoscale Conductivity Contrast by Scattering-Type Near-Field Optical Microscopy in the Visible, Infrared and THz Domains. *J. Infrared, Millimeter, Terahertz Waves* **2009**, *30*, 1255−1268.
(45) Stiegler, J. M.; Huber, A. J.; Diedenhofen, S. L.; Gómez Rivas, J.; Algra, R. E.; Bakkers, E. P. A. M.; Hillenbrand, R. Nanoscale Free-Carrier Profiling of Individual Semiconductor Nanowires by Infrared Near-Field Nanoscopy. *Nano Lett.* **2010**, *10*, 1387−1392.
(46) Dowdy, R. S.; Zhang, C.; Mohseni, P. K.; Fortuna, S. A.; Wen, J.-G.; Coleman, J. J.; Li, X. Perturbation of Au-Assisted Planar GaAs Nanowire Growth by P-Type Dopant Impurities. *Opt. Mater. Express* **2013**, *3*, 1687−1697.
(47) Oliver, R. A. Advances in AFM for the Electrical Characterization of Semiconductors. *Rep. Prog. Phys.* **2008**, *71*, 076501.
(48) Karbassi, A.; Ruf, D.; Bettermann, A. D.; Paulson, C. A.; van der Weide, D. W.; Tanbakuchi, H.; Stancliff, R. Quantitative Scanning near-Field Microwave Microscopy for Thin Film Dielectric Constant Measurement. *Rev. Sci. Instrum.* **2008**, *79*, 094706.
(49) Hudlet, S.; Saint Jean, M.; Guthmann, C.; Berger, J. Evaluation of the Capacitive Force between an Atomic Force Microscopy Tip and a Metallic Surface. *Eur. Phys. J. B* **1998**, *2*, 5−10.
(50) Buh, G. H.; Kopanski, J. J.; Marchiando, J. F.; Birdwell, A. G.; Kuk, Y. Factors Influencing the Capacitance−Voltage Characteristics Measured by the Scanning Capacitance Microscope. *J. Appl. Phys.* **2003**, *94*, 2680−2685.
(51) Williams, C. C. Two-Dimensional Dopant Profiling by Scanning Capacitance Microscopy. *Annu. Rev. Mater. Sci.* **1999**, *29*, 471−504.
(52) Abraham, D. W.; Williams, C.; Slinkman, J.; Wickramasinghe, H. K. Lateral Dopant Profiling in Semiconductors by Force Microscopy Using Capacitive Detection. *J. Vac. Sci. Technol., B: Microelectron. Process. Phenom.* **1991**, *9*, 703−706.
(53) Brotherton, S. D. Introduction. In *Introduction to Thin Film Transistors*; Springer, 2013; pp 1−5.
(54) Edwards, H.; Ukraintsev, V. A.; San Martin, R.; Johnson, F. S.; Menz, P.; Walsh, S.; Ashburn, S.; Wills, K. S.; Harvey, K.; Chang, M.-C. PN-Junction Delineation in Si Devices Using Scanning Capacitance Spectroscopy. *J. Appl. Phys.* **2000**, *87*, 1485−1495.
(55) Hemesath, E. R.; Schreiber, D. K.; Gulsoy, E. B.; Kisielowski, C. F.; Petford-Long, A. K.; Voorhees, P. W.; Lauhon, L. J. Catalyst Incorporation at Defects during Nanowire Growth. *Nano Lett.* **2012**, *12*, 167−171.
(56) Yang, Y.; Qi, J.; Liao, Q.; Zhang, Y.; Tang, L.; Qin, Z. Synthesis and Characterization of Sb-Doped ZnO Nanobelts with Single-Side Zigzag Boundaries. *J. Phys. Chem. C* **2008**, *112*, 17916−17919.
(57) Li, S.; Zhang, X.; Zhang, L.; Gao, M. Twinning-Induced Kinking of Sb-Doped ZnO Nanowires. *Nanotechnology* **2010**, *21*, 435602.
(58) Algra, R. E.; Verheijen, M. A.; Borgstrom, M. T.; Feiner, L.-F.; Immink, G.; van Enckevort, W. J. P.; Vlieg, E.; Bakkers, E. P. A. M. Twinning Superlattices in Indium Phosphide Nanowires. *Nature* **2008**, *456*, 369−372.
(59) Yang, B.; Liu, B.; Wang, Y.; Zhuang, H.; Liu, Q.; Yuan, F.; Jiang, X. Zn-Dopant Dependent Defect Evolution in GaN Nanowires. *Nanoscale* **2015**, *7*, 16237−16245.
(60) Chen, W.; Yu, L.; Misra, S.; Fan, Z.; Pareige, P.; Patriarche, G.; Bouchoule, S.; Cabarrocas, P. R. I. Incorporation and Redistribution of Impurities into Silicon Nanowires during Metal-Particle-Assisted Growth. *Nat. Commun.* **2014**, DOI: 10.1038/ncomms5134.
(61) Genovese, L.; Neelov, A.; Goedecker, S.; Deutsch, T.; Ghasemi, S. A.; Willand, A.; Caliste, D.; Zilberberg, O.; Rayson, M.; Bergman, A.; Schneider, R. Daubechies Wavelets as a Basis Set for Density Functional Pseudopotential Calculations. *J. Chem. Phys.* **2008**, *129*, 014109.
(62) Mohr, S.; Ratcliff, L. E.; Boulanger, P.; Genovese, L.; Caliste, D.; Deutsch, T.; Goedecker, S. Daubechies Wavelets for Linear Scaling Density Functional Theory. *J. Chem. Phys.* **2014**, *140*, 204110.

DOI: 10.1021/acsnano.6b06853
ACS Nano 2017, 11, 1530−1539

(63) Cherkashin, N.; Darras, F. X.; Pochet, P.; Reboh, S.; Ratel-Ramond, N.; Claverie, A. Modelling of Point Defect Complex Formation and Its Application to H+ Ion Implanted Silicon. *Acta Mater.* **2015**, *99*, 187−195.
(64) Takeuchi, S.; Suzuki, K. Stacking Fault Energies of Tetrahedrally Coordinated Crystals. *Phys. Status Solidi A* **1999**, *171*, 99−103.
(65) Ebert, P.; Zhang, T.; Kluge, F.; Simon, M.; Zhang, Z.; Urban, K. Importance of Many-Body Effects in the Clustering of Charged Zn Dopant Atoms in GaAs. *Phys. Rev. Lett.* **1999**, *83*, 757−760.

DOI: 10.1021/acsnano.6b06853
ACS Nano 2017, 11, 1530−1539